Highly Sensitive Salinity and Temperature Sensor Using Tamm Resonance

Zaky A. Zaky (zaky.a.zaky@science.bsu.edu.eg)
Beni Suef University Faculty of Science https://orcid.org/0000-0002-8300-7755
Arafa H. Aly
Beni Suef University Faculty of Science

Research Article

Keywords: Salinity Sensor, Temperature sensor, Seawater, Photonic crystal, Tamm resonance, Functionalized biosensors

Posted Date: March 10th, 2021

DOI: https://doi.org/10.21203/rs.3.rs-300379/v1

Version of Record: A version of this preprint was published at Plasmonics on July 7th, 2021. See the published version at https://doi.org/10.1007/s11468-021-01487-6.

Highly Sensitive Salinity and Temperature Sensor Using Tamm Resonance

ZAKY A. ZAKY*, AND ARAFA H. ALY

TH-PPM Group, Physics Department, Faculty of Sciences, Beni-Suef University, Egypt

* Corresponding author: zaky.a.zaky@science.bsu.edu.eg, zaky.a.zaky92@gmail.com

Abstract:

In this paper, a Tamm plasmons resonance-based sensor is theoretically studied to calculate the salinity of seawater as well as a temperature sensor based on photonic crystals. The transfer matrix method (TMM) is used to systematically study and analyze the reflected s-polarized electromagnetic waves from the sensing structure. The proposed structure composes of prism/Au/water/$(Si/SiO_2)^N$/Si. The sensitivity, figure-of-merit, quality factor, and detection limit of the sensors are improved by optimizing the thickness of the seawater layer, incident angle, salinity concentration, and temperature. The proposed salinity sensor records a very high sensitivity of $8.5x10^4$ nm/RIU and quality factor of $3x10^3$, and a very low detection limit of 10^{-7} nm. Besides, the suggested temperature sensor achieves high sensitivity (from 2.8 nm/˚C to 10.8 nm/˚C), high-quality factor of $3.5x10^3$, and a very low detection limit of $3x10^{-7}$ nm. These results indicate that the proposed sensor is a strong candidate for salinity and temperature measurements.

Keywords: Salinity Sensor; Temperature sensor; Seawater; Photonic crystal; Tamm resonance; Functionalized biosensors.

1. Introduction

Water is an essential need for living organisms to stay alive and is one of the most serious global issues facing the world today [1]. The polluted water causes various diseases such as cholera, typhoid, and other water-borne diseases [2]. Salinity is the salts that dissolved in the water and is one of the water contaminations [3]. The phase of salinity measuring is very important to determine the accuracy of water desalination systems. Besides, the temperature and salinity of seawater are very important in the physical oceanography [4].

Recently, more attention has been paid to develop salinity and temperature sensors. In 2009, Possetti et al. [5] proposed an in-fibre Mach–Zehnder interferometer. A theoretical sensitivity for salinity measurements of 46.5 nm/RIU and thermal sensitivity of 53 pm/˚C were obtained. In 2014, Kamil et al [6] experimentally demonstrated a method for salinity sensors using tapered single-mode fibre. They reported a sensitivity of 2834.3 nm/RIU. In 2018, a salinity sensor using photonic crystal fibre (PCF) was reported by Vigneswaran et al [3]. This sensor recorded a sensitivity of 5675 nm/RIU. In 2019 [7], Amiri et al. proposed a temperature-salinity tri-core PCF sensor with a salinity sensitivity of 5674 nm/RIU, and temperature sensitivity is 4 nm/˚C. In 2020, Akter et al. [8] designed a dual-core microstructure PCF as a temperature and salinity sensor. They achieved salinity sensitivity 11111.11 nm/RIU and temperature sensitivity 1000 pm/°C.

The photonic crystal (PC) is a multi-layer structure with a different dielectric constant in a periodic structure [9-11]. PC can be divided according to its periodicity into one dimensional (1D-PC), two dimensional (2D-PC), and three dimensional (3D-PC) [12-18]. PC manipulates the light propagation through it. When the incident light propagates through the PC, it reflects at each interface. Under a suitable condition, constructive interference between

the reflected waves occurs, and the resultant reflected wave destructively interferes with the incident wave. Due to this destructive interference, a forbidden bandgap appears (PBG) [19-21].

In 2007, Tamm plasmons (TP) was introduced [22,23]. It is confinement of electromagnetic waves at the interface between 1D-PC and the metallic layer. A TP resonant dip appears inside the PBG. The position of TP dip is very sensitive to the optical properties of the PC and the surrounding [24]. So, the TP structure can be used as a sensor [25].

However, PCF has attracted more attention in most of the previous salinity and temperature studies, it needs a complex manufacturing process and additional equipment to achieve the machining process requirements. Also, the quality of the system depends upon several parameters such as group birefringence, phase, and fringes interference [26,27]. So, we suggest in this manuscript a quite simple and ultra-sensitive one-dimensional photonic crystal structure based on Tamm resonance.

The transfer matrix method (TMM) will be used to systematically study the reflected s-polarized electromagnetic waves from the sensing structure by using MATLAB tools.

2. Sensor geometry

The structural parameters of the whole structure (prism/Au/water/$(Si/SiO_2)^N$/Si) of the sensor is indicated in Fig. 1. It consists of 1D-PC coated with a metallic layer (Au layer). The water layer is presented between the 1D-PC and the metallic layer that is deposited on the prism face to prevent the metallic layer from floating into the water layer. The TE-polarized light incident with angle α_0 from one lateral prism-face to its base and reflected out from the other face, and analysed by a photodetector [28].

The water layer can be done experimentally by depositing any suitable layer with the desired dimensions instead. Then, this layer can be easily removed with a strong acid (etching process). Plasma-enhanced chemical vapor deposition (PECVD), spin-coating [29], spray pyrolysis, thermal evaporation, and some other deposition techniques can be used to deposit dielectric (Si/SiO_2) homogeneous films [30-32]. Therefore, the convenient and practical qualities to manufacture are taken into account.

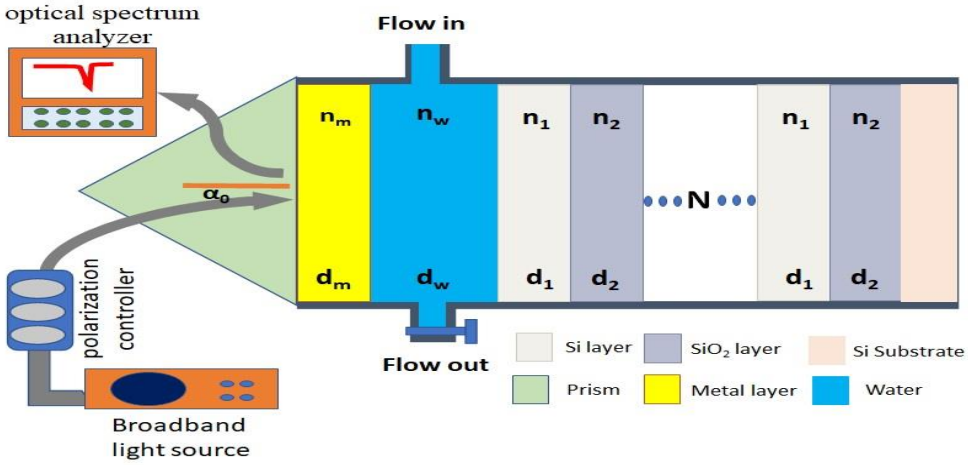

Figure 1: Schematic illustration and experimental setup of the suggested sensor consisting of prism/Au/ water/$(Si/SiO_2)^N$/Si.

The PC is periodically arranged by Si-layer and SiO_2-layer. The thickness of Si (d_1), SiO_2 (d_2), Au (d_m), and the water layer (d_w) are 100 nm, 400 nm, 25 nm, and 700 nm, respectively. The refractive index of the substrate is 3.3.

A significant factor influencing the performance of the proposed sensor is the adjusting of the refractive index of the prism. Leiming et al. reported a SPR sensor and concluded that the highest sensitivity can be achieved using a low refractive index prism [33]. Therefore, the refractive index of the prism in this study will be 1.5.

3. Numerical method

The TMM will be used to systematically study the reflected S-polarized electromagnetic waves from the structure by using MATLAB tools. For the s-polarized wave, the transfer matrix ($\boldsymbol{G}$) of the structure is:

$$\boldsymbol{G} = \begin{pmatrix} G_{11} & G_{12} \\ G_{21} & G_{22} \end{pmatrix} = (\boldsymbol{g}_m)(\boldsymbol{g}_1\boldsymbol{g}_2)^N, \tag{1}$$

where G_{11}, G_{12}, G_{21}, and G_{22} are the elements of the total matrix of the structure. $\boldsymbol{g}_m$, $\boldsymbol{g}_1$, and $\boldsymbol{g}_2$ are the transfer matrix for the metallic layer (Au), Si, and SiO_2, respectively as the following:

$$\begin{aligned} \mathbf{g}_m &= \begin{pmatrix} \cos\delta_m & -\frac{i\ \sin\delta_m}{p_m} \\ -ip_m\sin\delta_m & \cos\delta_m \end{pmatrix}, \\ \mathbf{g}_1 &= \begin{pmatrix} \cos\delta_1 & -\frac{i\ \sin\delta_1}{p_1} \\ -ip_1\sin\delta_1 & \cos\delta_1 \end{pmatrix}, \\ \mathbf{g}_2 &= \begin{pmatrix} \cos\delta_2 & -\frac{i\ \sin\delta_2}{p_2} \\ -ip_2\sin\delta_2 & \cos\delta_2 \end{pmatrix}, \end{aligned} \tag{2}$$

where the phase differences (δ) at the Au, Si, and SiO_2 layers are given by;

$$\delta_m = \frac{2\pi n_m d_m \cos\theta_m}{\lambda},\ \beta_1 = \frac{2\pi n_1 d_1 \cos\theta_1}{\lambda}, \text{ and } \beta_2 = \frac{2\pi n_2 d_2 \cos\theta_2}{\lambda}, \tag{3}$$

the values of p for the TE wave are given by $p_i = n_i \cos\theta_i\ (i = 1{,}2 \text{ and } m)$, and θ is the incident angle.

Chebyshev polynomials of the second kind are used to calculate the matrix for N periods [34]. More details can be found in our previous studies [35-37]. The reflectance spectra of the proposed structure can be given as [38]:

$$R = |r^2|, \tag{4}$$

where r denotes the reflection coefficient of the structure ($r = \frac{(G_{11}+G_{12}p_s)p_p-(G_{21}+G_{22}p_s)}{(G_{11}+G_{12}p_s)p_p+(G_{21}+G_{22}p_s)}$), $p_p = n_p \cos j_p$(for prism), and $p_s = n_s \cos j_s$(for substrate).

The 1D-PC is designed with two different dielectric layers (Si and SiO_2). The thermal expansion and thermo-optic effects are taken into account to achieve an accurate simulation. The refractive index of Si and SiO_2 as a function of temperature can be calculated as the following:

$$n = n_0 + \beta n_0(\Delta T), \tag{5}$$

where n_0 is the refractive index of Si (3.3) and SiO_2 (1.46) at room temperature, and β is the thermo-optic coefficient for Si (1.86×10^{-4} /°C) and SiO_2 (6.8×10^{-6} /°C). ΔT is the variation of the temperature. The term ($\beta n_0 \Delta T$) indicates the change in the refractive index of the layer with the change of temperature. Also, the thickness of layers changes with the temperature as the following:

$$d = d_0 + \gamma d_0(\Delta T), \tag{6}$$

where d_0 is the room temperature thickness of each layer, γ is the thermal expansion coefficient of Si (0.5×10^{-6} /°C) and SiO_2 (2.6×10^{-6} /°C) [39].

Drude model is used in the calculation of dielectric constant of Au layer ($\sqrt{n_m}$) as the following [40]:

$$n_m = \sqrt{1 - \frac{\omega_p^2}{\omega(\omega + i\emptyset)}}, \tag{7}$$

where ω_p, $\emptyset$, and ω is plasma frequency, damping frequency, and frequency of the incident light, respectively [24].

As a function of salinity concentration(C_s in %), temperature (T in ˚C) , and wavelength (λ in nm), the index of refraction of seawater is calculated as the following [41,3,8]:

$$\begin{aligned} n(C_s, \lambda, T) = {} & 1.3104 + (1.779 \times 10^{-4} - 1.05 \times 10^{-6}\mathrm{T})C_s + 1.6 \\ & \times 10^{-8} T^2 C_s - \frac{4382}{\lambda^2} - 2.02 \times 10^{-6} T^2 \\ & + \frac{15.868 + 0.01155\, C_s - 0.00423\mathrm{T}}{\lambda} + \frac{1.1455 \times 10^{-6}}{\lambda^3}. \end{aligned} \tag{8}$$

4. Simulation results and discussions

Now, we study the simulation analysis of the incident waves into the proposed sensor and the effect of the metal layer. The structure is composed of prism/Au/water/$(Si/SiO_2)^N$/Si. In Fig. 2, the black and red curves are the reflectance spectra of the prism/water/$(Si/SiO_2)^N$/Si and prism/Au/water/$(Si/SiO_2)^N$/Si structures, respectively. In the absence of the Au layer, A PBG was expanded from 1514 nm to 2381 nm, because of the system periodicity.

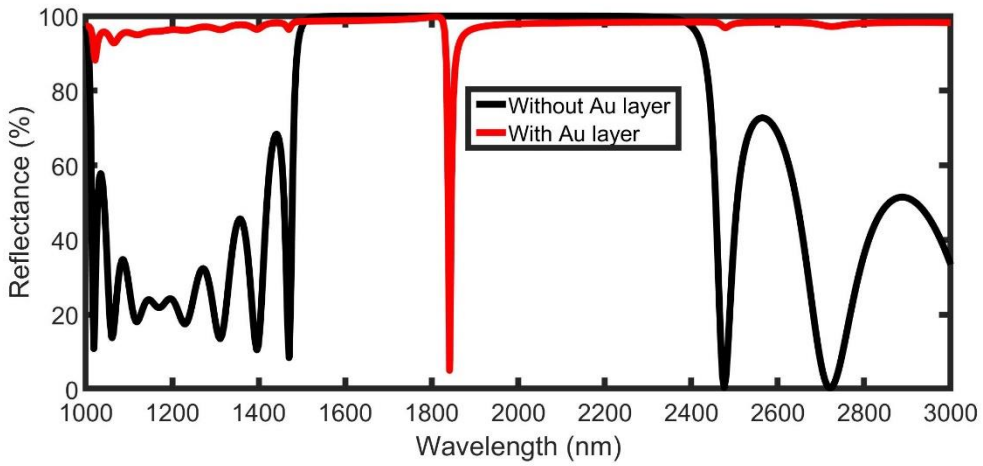

Figure 2: Reflectance spectra for prism/water/$(Si/SiO_2)^N$/Si and prism/Au/ water/$(Si/SiO_2)^N$/Si versus the wavelength with α_0=0˚, *N*=8, d_w=700 nm, C_s= 0 %, T=25 ˚C, and d_m=25 nm.

On the contrary of surface plasmon, Tamm resonance has the ability to direct excite at normal incidence by adding an Au layer in front of the 1D-PC. Between the Au surface and 1D-PC, the electromagnetic modes are confined at wavelength 1841 nm (red line in Fig. 2).

4.1. Salinity sensor:

In this section, the effect of the change of salinity concentration on the resonant dip position will be studied. As clear in Fig. 3, and according to Eq. 6, the refractive index of water increased with the change of salinity concentration in water. Because the position of the Tamm resonant dip depends on the effective index of refraction of 1D-PC and the surrounding, the dip position is shifted with any increase or decrease in the water refractive index.

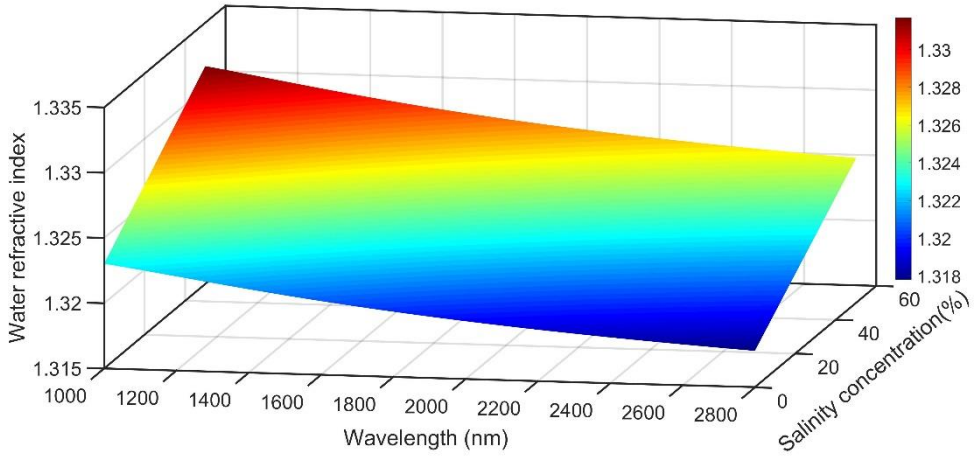

Figure 3: Dependence of water refractive index on both wavelength and salinity concentration at room temperature (25 ˚C).

It is important to keep in mind that a small change in salinity concentration would cause a resonant dip wavelength (λ_r) shift. The darker the reflectivity (zero reflectance), the sharper the dip-position jump [42]. So, even a very small change in the refractive index due to the salinity concentration change can be detected by a sharp dip shift relative to the calibration medium (pure water), as shown in Fig. 4.

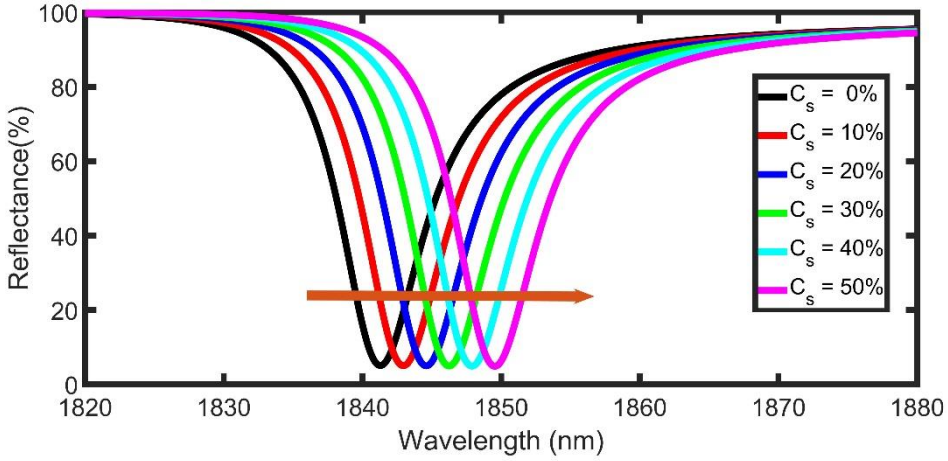

Figure 4: Reflectance spectra for prism/Au/water/$(Si/SiO_2)^N$/Si as a function of the wavelength at different salinity concentrations with α_0=0˚, N=8, d_w=700 nm, T=25 ˚C, and d_m=25 nm.

Fig. 4 shows the reflectance variation versus the incident wavelength for different values of salinity concentration. As the salinity concentration increases from 0 % to 50 %, the dip position is red-shift to a higher wavelength from 1841.26 nm to 1849.58nm with a change in wavelength equal to 8.32 nm.

Effect of the water layer thickness on the salinity sensor performance:

As clear in Fig. 5, the Tamm resonance wavelength (λ_r) has a large red-shift with the increase of the water layer thickness at a fixed incident angle, Au thin film thickness, and temperature that is due to the increasing of the geometric path of the light wave inside the water layer. Consequently, the coupling between the incident light and water components is enhanced. It is clear from Fig. 5 that the wavelength shifts rapidly improved from 8.32 nm to 12.68 nm with the increase of water layer thickness from 700 nm to 6000 nm but slightly increases with further increase in water thickness. So, the water layer thickness of 6000 nm will be the optimum thickness. This result is in agreement with prior experimental and theoretical studies [43-45].

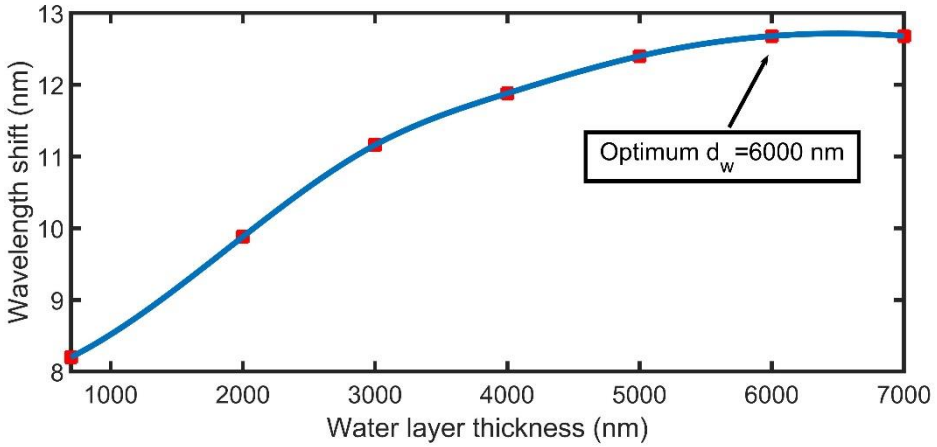

Figure 5: The relation between the thickness of the water layer and wavelength shift at N = 8, d_m = 25 nm, T=25 ˚C, and α_0=0˚.

Effect of the incident angle on the salinity sensor:

As clear in Fig. 6(A), the PBG becomes broader and is blue-shifted to lower wavelengths with the increase of the incident angle. Besides, total internal reflection (TIR) occurs with a critical angle (φ_c) of 61.6˚ according to TIR principle:

$$\varphi_c = \sin^{-1}\left(\frac{n_{\text{water}}}{n_{\text{prism}}}\right) \tag{9}$$

When the angle of wave propagation increases from 0˚ to 50˚, the wavelength shift slightly increases. In contrast, a rapid increase in the wavelength shift with the increase of the angle from 50˚ to 61.6˚, as clear in Fig. 6(B). This jump in the wavelength shift is because the geometrical path of the waves increases with the same behaviour with the increase of the incident angle that causes good confinement through the water molecules [35]. Therefore, the angle of 61.6˚ will be the optimum angle.

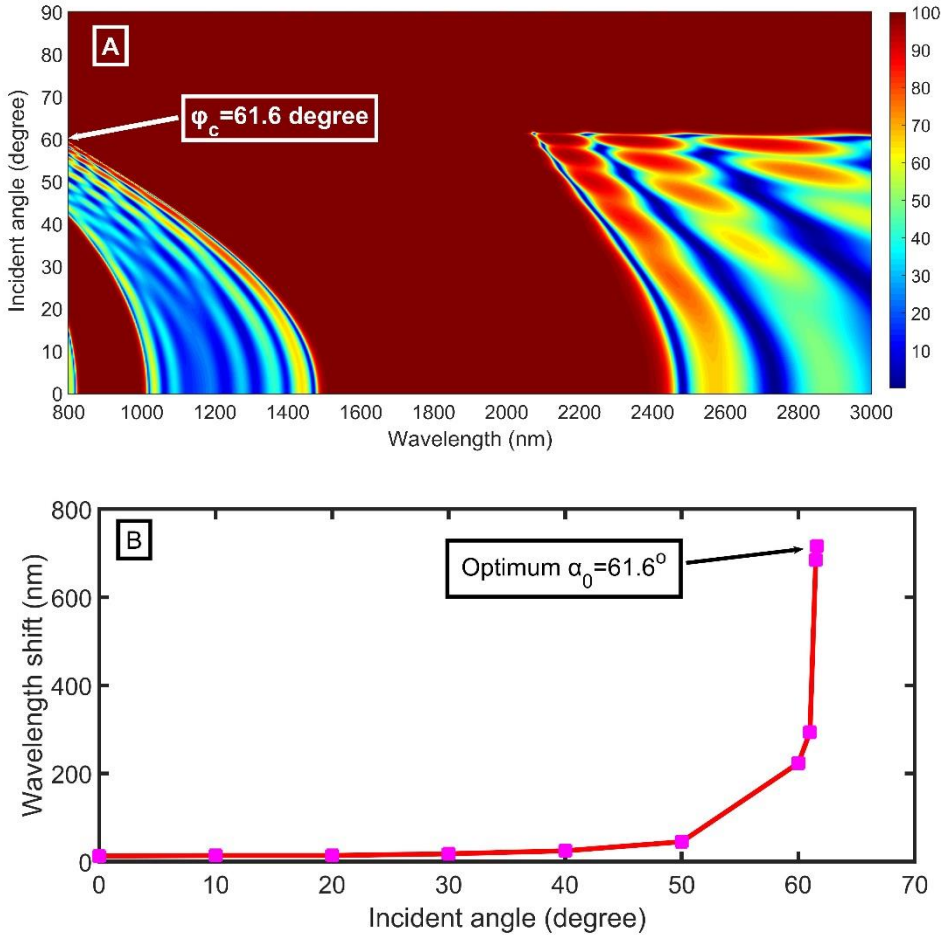

Figure 6: (A) The variation of reflectance as a function of wavelength and incident angle. (B) The relation between the incident angle and wavelength shift at N = 8, d_m= 25 nm, d_w= 6000 nm, and T=25 ˚C.

Effect of the operating temperature on the salinity sensor:

As shown in Fig. 7, by increasing the operating temperature from 0 ˚C to 15 ˚C, the wavelength shift decreases from 733.8 nm to 707.8 nm. Then, the wavelength shift increases from 707.8 nm to 717.1 nm with the increase of temperature from 15 ˚C to 25 ˚C. For further increase in temperature, the resonance dip goes out from the wavelength range of concern.

Although the performance of the salinity sensor at 0 ˚C is slightly better than the performance at 25 ˚C, we will consider room temperature (25 ˚C) as the optimum condition to conserve the energy consumed in the cooling process in our country.

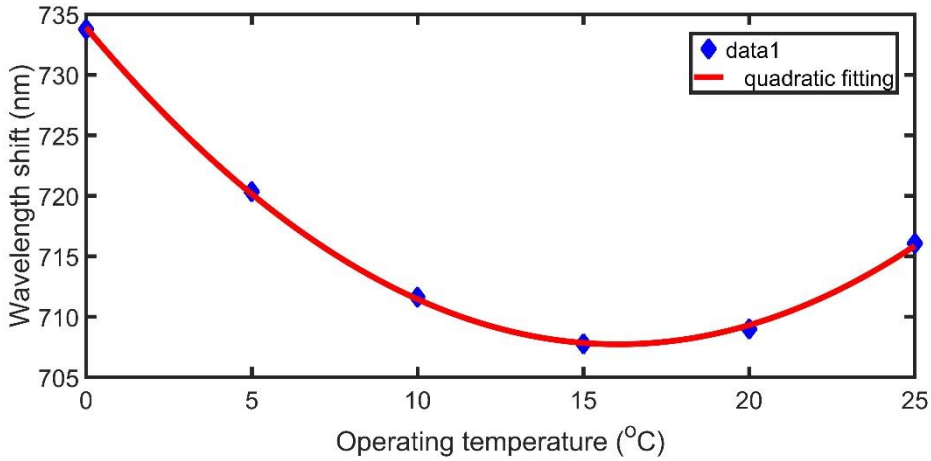

Figure 7: The effect of operating temperature on the performance of the salinity sensor at $N = 8$, $d_m = 25$ nm, $d_w = 6000$ nm, and $\alpha_0 = 61.6^{\circ}$.

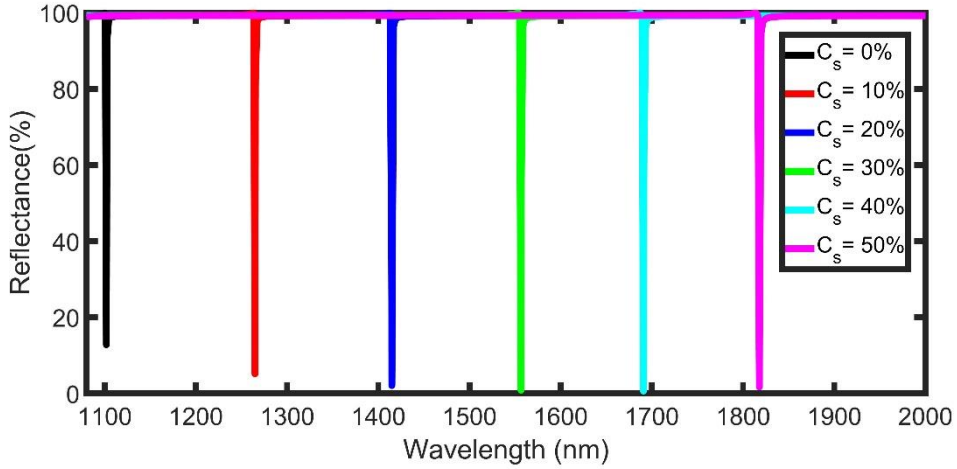

Figure 8: Reflectance of the salinity sensor at $\alpha_0 = 61.6^{\circ}$, $N = 8$, $d_w = 6000$ nm, $T = 25$ ˚C, and $d_m = 25$ nm.

The reflectance spectra of the proposed sensor at the optimum conditions are cleared in Fig. 8. Unlike previous studies of PCF **[3,8]**, and like multilayer photonic crystals [35], the resonant dip is red-shifted to high wavelengths with the salinity increase. by raising the salinity from 0 % to 50 %, the dip position moves to the right to lower energy radiation having a wavelength shift from 1101.8 nm to 1817.8 nm.

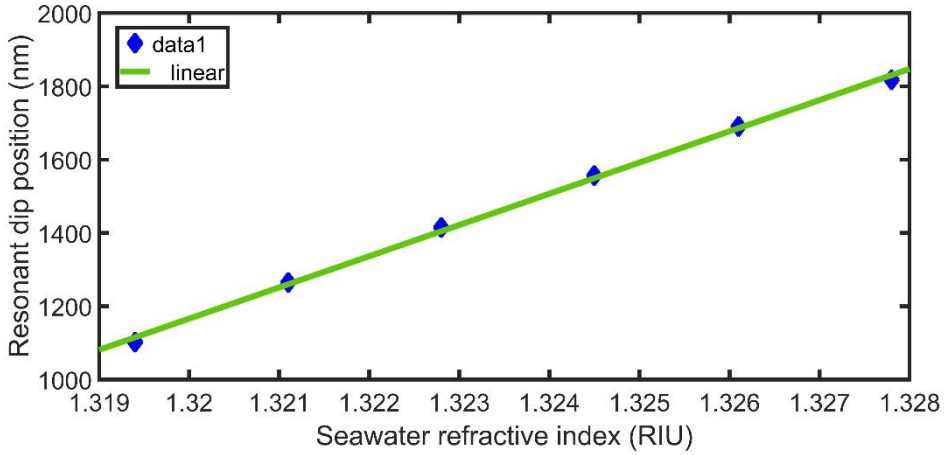

Figure 9: The linear relation between the refractive index of seawater and resonant dip position at optimum conditions.

Now, significant factors like sensitivity (*S*), quality factor (*QF*), the figure of merit (*FoM*), and detection limit (*DL*) are calculated for the salinity sensor in Table 1. Sensitivity is the ratio between the wavelength shift of the dip and the variation in the water refractive index as the following:

$$S = \frac{\Delta\lambda_{\mathrm{r}}}{\Delta n}, \tag{10}$$

FoM depends on both sensitivity and the bandwidth ($FWHM$) of resonant dips as the following:

$$FoM = \frac{S}{FWHM} \tag{11}$$

The quality factor is the ratio between the resonant dip position and $FWHM$ as:

$$QF = \frac{\lambda_{\mathrm{r}}}{FWHM} \tag{12}$$

The detection limits denoting the smallest measurable refractive index of salinity concentration change according to:

$$DL = \frac{\lambda_{\mathrm{r}}}{20\ S\ QF} \tag{13}$$

The result in Fig. 9 shows that the shift of the resonant dip position in the case of salinity measurements is linearly proportional to the change in the index of refraction of seawater. The green line in Fig. 9 is the linear fitting of the data that indicates a fixed value of sensitivity ($8.5\text{x}10^4$ nm/RIU) as the following equation:

$$\lambda_{\mathrm{r}} = \ 85000\, n - 110000 \quad (\mathrm{R}^2 = 0.99) \tag{14}$$

This linearity of data emphasizes the stability and rationality of the proposed salinity sensor. The proposed sensor recorded a very high sensitivity of $8.5\text{x}10^4$ nm/RIU and quality factor of $3\text{x}10^3$, and a very low detection limit of a minimum detectable dip position shift is about $3\text{x}10^{-7}$ nm. These results indicate that the suggested sensor is a strong candidate for salinity measurements than previous studies as clear in Table 3.

Table 1: The sensitivity (S_s), quality factor (QF), figure of merit (FoM) at the optimum conditions of the salinity sensor.

C_s (%)	n (RIU)	λ_r (nm)	S_s (nm/RIU)	$FWHM$ (nm)	$FoM\times10^5$ (/RIU)	$QF\times10^3$
0	1.3194	1101.8	------	0.30	------	3.7
10	1.3211	1264.8	95882	0.35	2.8	3.6
20	1.3228	1414.8	92059	0.41	2.3	3.5
30	1.3245	1556.5	89157	0.48	1.9	3.3
40	1.3261	1690.8	87911	0.54	1.6	3.1
50	1.3278	1817.8	85238	0.60	1.4	3.0

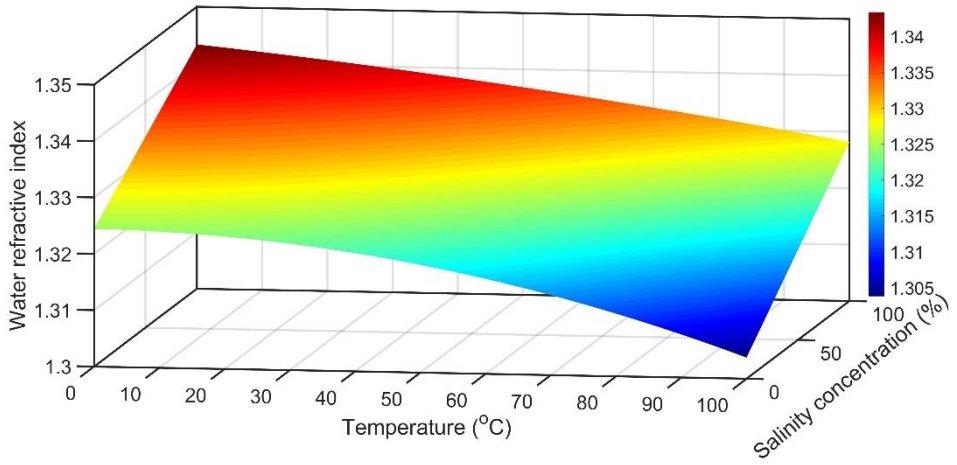

Figure 10: Dependence of water refractive index on both temperature and salinity concentration at a wavelength of 1000 nm.

4.2. Temperature sensor:

In this section, the effect of the temperature variation on the resonant dip position will be studied. As clear in Fig. 10, and according to Eq. 6, the refractive index of water changes with the change of seawater temperature.

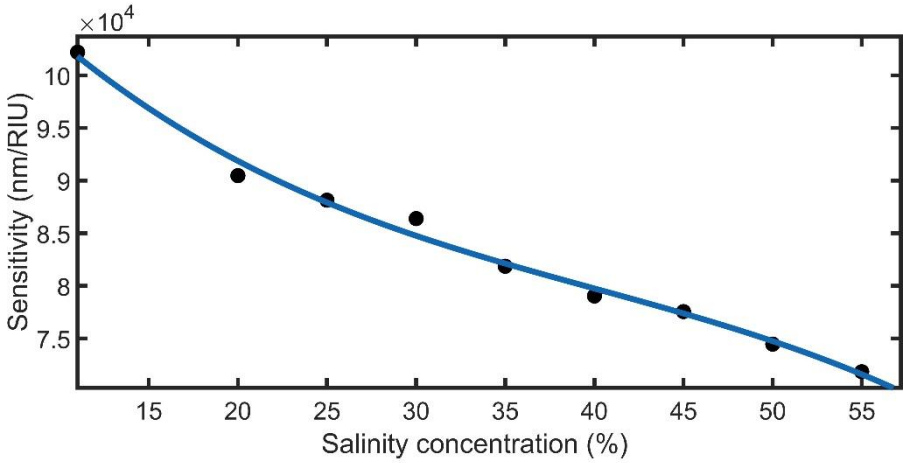

Figure 11: The effect of salinity concentration on the sensitivity of the temperature sensor at the optimum conditions.

At a salinity concentration of 0 % and wavelength of 1000 nm, with the increase of the operating temperature from 0 ˚C to 100 ˚C, the refractive index of seawater decreases from 1.3247 to 1.304 ($\Delta n = 0.0207$). But, at a salinity concentration of 100 % and wavelength of 1000 nm, with the increase of the operating temperature from 0 ˚C to 100 ˚C, the refractive index of seawater decreases from 1.3433 to 1.3282 ($\Delta n = 0.0151$). This means that seawater is more sensitive to temperature with a decrease in salinity concentration.

Fig. 11 demonstrates the relationship between sensitivity and salinity concentration from 11 % to 55 %. Below concentration 11 %, the resonant dips are blue-shifted and go out from the wavelength range of concern. So, the salinity concentration of 11 % will be the optimum salinity for the proposed temperature sensor. The blue line in Fig. 11 is the polynomial fitting of three-degree order like the following:

$$S_{\mathrm{T}} = -0.3498\, C_{\mathrm{s}}^3 + 42.01\, C_{\mathrm{s}}^2 + -2147\, C_{\mathrm{s}} + 1.208 \times 10^5 \quad (15)$$

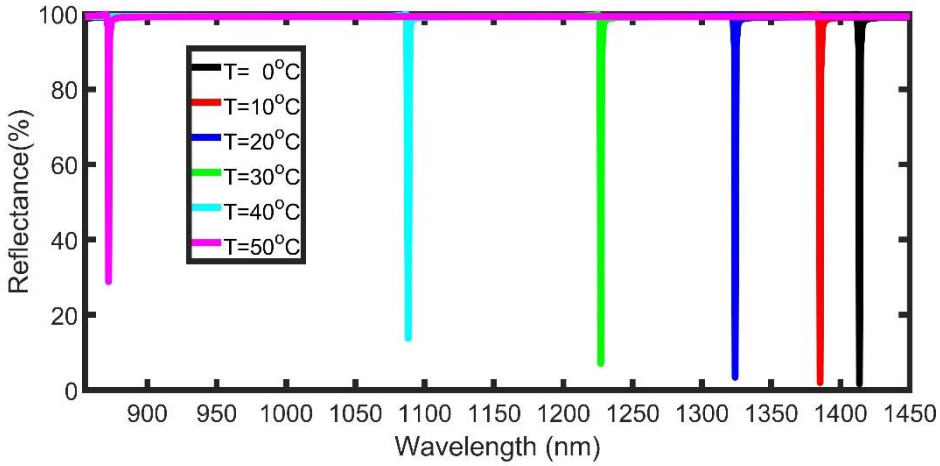

Figure 12: Reflectance spectra of the proposed structure as a temperature sensor as a function of the wavelength at different Temperatures with α_0 =61.6°, N=8, d_w=6000 nm, C_s=11 %, and d_m=25 nm.

The plotted reflectance spectra in Fig. 11 illustrates that any change in the operating temperature will be translated into a shift in the resonant dip recorded at the optical analyser. As the operating temperature increases from 0 ˚C to 50 ˚C, the dip position is blue-shifted from 1413.6 nm to 872.0 nm. For temperatures higher than 50 ˚C, the resonant dip will overlap with the neighbour dips. So, we will end our study at 50 ˚C.

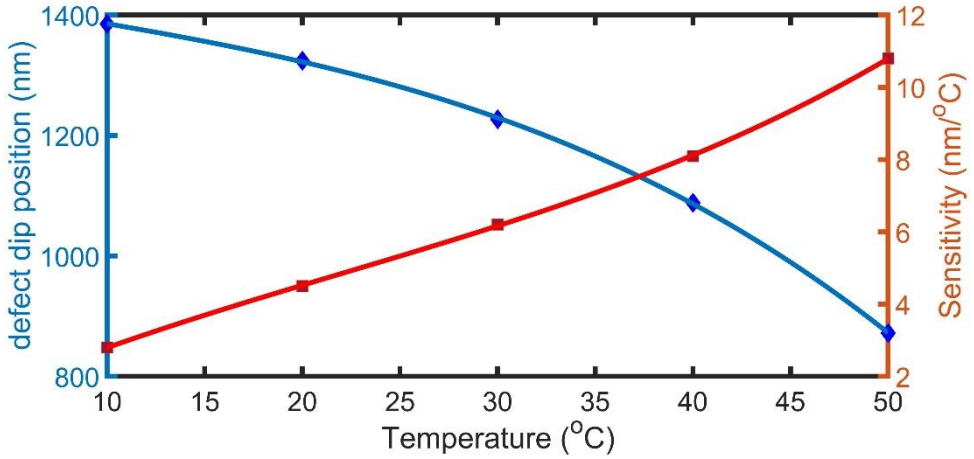

Figure 13: defect dip position and sensitivity of the proposed temperature sensor as a function of temperature at optimum conditions.

Table 2: The sensitivity (*S*), quality factor (*QF*), figure of merit (*FoM*) at the optimum conditions of the temperature sensor.

T (˚C)	n (RIU)	λ_r (nm)	S_T (nm/RIU)	S_T (nm/˚C)	$FWHM$ (nm)	$FoM\times10^5$ (/RIU)	$QF\times10^3$
0	1.3228	1413.6	-----	-----	0.41	1.8	3.5
10	1.3224	1385.3	70750	2.8	0.39	2.4	3.5
20	1.3218	1324.0	89600	4.5	0.37	2.6	3.6
30	1.3207	1227.1	88810	6.2	0.34	3.1	3.6
40	1.3193	1088.2	92971	8.1	0.30	3.2	3.7
50	1.3175	872.0	102189	10.8	0.32	1.8	2.7

Table 3: comparison between our proposed salinity-temperature sensor and previously proposed sensors.

Structures	S_s (nm/%)	S_s (nm/RIU)	S_T (nm/RIU)	S_T (nm/˚C)	Ref.
SPR temperature sensor (2012)	---	---	---	0.72	[46]
microfiber knot resonator	0.21	---	---	---	[47]
PCF salinity sensor (2018)	---	5675	---	---	[3]
SPR temperature sensor (2018)	---	---	4613	1.55	[48]
FEM based dual core temperature sensor (2019)	---	----	---	0. 82	[49]
dual-core PCF microstructure (2020)	2	11111	2000	1	[8]
Our work	14.32	85000	70750 to 102189	2.8 to 10.8	

Fig. 13 shows the non-linearity (non-fixed sensitivity) of the proposed temperature sensor as in the previous studies **[8,7]**. The proposer sensor is more sensitive to high temperature (10.8 nm/˚C) more than low temperature (2.2 nm/˚C). Table 2 demonstrates that the proposed temperature sensor at these conditions recorded a very high sensitivity and quality factor, and a very low detection limit ($2\text{x}10^{-7}$). Table 3 introduces a comparison between the

proposed salinity-temperature sensor and the previously proposed sensors. The performance of the suggested sensor in terms of sensitivity is better compared with the previous sensors. Besides, this sensor has many advantages because of the low cost, simple structure, very high sensitivity, and flexibility.

5. Conclusion

In this paper, we proposed a theoretical analysis of salinity and temperature measurements through a 1D-PC platform using Tamm resonance. The seawater layer thickness, the incident angle of electromagnetic wave, the operating temperature of the salinity sensor, and salinity concentration in temperature sensor were optimized at 6000nm, 61.6°, 25 ˚C, and 11 %, respectively. The proposed sensor has a narrower *FWHM* of about 0.34 nm with ultra-high sensitivity of $8.5x10^4$ nm/RIU for salinity concentration, and sensitivity from 2.8 nm/˚C to 10.8 nm/˚C for the temperature sensor. The linearity between salinity concentration and the Tamm resonant dip enables the proposed structure to detect salinity concentration effectively. Although the relation between the Tamm resonant dip and temperature change in temperature sensor, it achieved high sensitivity that distinguished it. Fig. 7 clear that the proposed salinity sensor is slightly sensitive in cold countries.

Funding

The authors declare no Fund.

Disclosures

The authors declare no conflicts of interest.

Correspondence

Requests for materials or code should be addressed to Z.A.Z.

Author contributions

Z.A. Zaky performed numerical simulations, analyzed the data, discussed the results and wrote the main manuscript text. A.H. Aly analyzed the data, discussed the results and supervised this work.

ORCID

https://orcid.org/0000-0002-8300-7755 (Z. A. Zaky)

https://orcid.org/0000-0003-0795-378X (A. H. Aly)

References

1. Xie Z, Duo Y, Lin Z, Fan T, Xing C, Yu L, Wang R, Qiu M, Zhang Y, Zhao Y (2020) The rise of 2D photothermal materials beyond graphene for clean water production. Adv Sci 7 (5):1902236

2. Hakami BA (2015) Impacts of Soil and Water Pollution on Food Safety and Health Risks. Technology 6 (11):32-38

3. Vigneswaran D, Ayyanar N, Sharma M, Sumathi M, Rajan M, Porsezian K (2018) Salinity sensor using photonic crystal fiber. Sens Actuator A-Phys 269:22-28

4. Wang S, Liao Y, Yang H, Wang X, Wang J (2015) Modeling seawater salinity and temperature sensing based on directional coupler assembled by polyimide-coated micro/nanofibers. Appl Optics 54 (34):10283-10289

5. Possetti G, Kamikawachi R, Prevedello C, Muller M, Fabris J (2009) Salinity measurement in water environment with a long period-grating based interferometer. Meas Sci Technol 20 (3):034003

6. Kamil YM, Bakar MA, Syahir A, Mahdi M Determining salinity using a single-mode tapered optical fiber. In: 2014 IEEE 5th International Conference on Photonics (ICP), 2014. IEEE, pp 223-226

7. Amiri IS, Paul BK, Ahmed K, Aly AH, Zakaria R, Yupapin P, Vigneswaran D (2019) Tri-core photonic crystal fiber-based refractive index dual sensor for salinity and temperature detection. Microw Opt Technol Lett 61 (3):847-852

8. Akter S, Ahmed K, El-Naggar SA, Taya SA, Nguyen TK, Dhasarathan V (2020) Highly Sensitive Refractive Index Sensor for Temperature and Salinity Measurement of Seawater. Optik:164901

9. Prabu K, Nasre D (2019) Design and Analysis of a Novel Optical Circulator Based on Photonic Crystal for Photonic Integrated Circuit Applications. Plasmonics 14 (5):1261-1267

10. Ahmed AM, Elsayed HA, Mehaney A (2020) High-Performance Temperature Sensor Based on One-dimensional Pyroelectric Photonic Crystals Comprising Tamm/Fano Resonances. Plasmonics:1-11

11. Joannopoulos JD, Villeneuve PR, Fan S (1997) Photonic crystals: putting a new twist on light. Nature 386 (6621):143-149

12. Yablonovitch E (1987) Inhibited spontaneous emission in solid-state physics and electronics. Phys Rev Lett 58 (20):2059

13. Shaban SM, Mehaney A, Aly AH (2020) Determination of 1-propanol, ethanol, and methanol concentrations in water based on a one-dimensional phoxonic crystal sensor. Appl Optics 59 (13):3878-3885

14. Abadla MM, Elsayed HA (2020) Detection and sensing of hemoglobin using one-dimensional binary photonic crystals comprising a defect layer. Appl Opt 59 (2):418-424

15. Aly AH, El-Naggar SA, Elsayed HA (2015) Tunability of two dimensional n-doped semiconductor photonic crystals based on the Faraday effect. Opt Express 23 (11):15038-15046

16. Abadla MM, Tabaza NA, Tabaza W, Ramanujam N, Wilson KJ, Vigneswaran D, Taya SA (2019) Properties of ternary photonic crystal consisting of dielectric/plasma/dielectric as a lattice period. Optik 185:784-793

17. Abd El-Ghany SE, Noum WM, Matar Z, Zaky ZA, Aly AH (2020) Optimized bio-photonic sensor using 1D-photonic crystals as a blood hemoglobin sensor. Phys Scr 96 (3):035501

18. Zi J, Li S, Chen H, Li J, Li H (2016) Photonic crystal fiber polarization filter based on surface plasmon polaritons. Plasmonics 11 (1):65-69

19. Yablonovitch E (2001) Photonic crystals: semiconductors of light. SciAm 285 (6):46-55

20. Aly AH, Sayed FA, Elsayed HA (2020) Defect mode tunability based on the electro-optical characteristics of the one-dimensional graphene photonic crystals. Appl Optics 59 (16):4796-4805

21. Nouman WM, Abd El-Ghany S, Sallam SM, Dawood AFB, Aly AH (2020) Biophotonic sensor for rapid detection of brain lesions using 1D photonic crystal. Opt Quantum Electron 52 (6)

22. Kaliteevski M, Iorsh I, Brand S, Abram R, Chamberlain J, Kavokin A, Shelykh I (2007) Tamm plasmon-polaritons: Possible electromagnetic states at the interface of a metal and a dielectric Bragg mirror. Phys Rev B 76 (16):165415

23. Sasin M, Seisyan R, Kalitteevski M, Brand S, Abram R, Chamberlain J, Egorov AY, Vasil'Ev A, Mikhrin V, Kavokin A (2008) Tamm plasmon-polaritons: Slow and spatially compact light. Appl Phys Lett 92 (25):251112

24. Ahmed AM, Mehaney A (2019) Ultra-high sensitive 1D porous silicon photonic crystal sensor based on the coupling of Tamm/Fano resonances in the mid-infrared region. Sci Rep 9 (1):6973

25. Zaky ZA, Aly AH (2020) Theoretical study of a tunable low-temperature photonic crystal sensor using dielectric-superconductor nanocomposite layers. Journal of Superconductivity and Novel Magnetism. doi:10.1007/s10948-020-05584-1

26. Villatoro J, Finazzi V, Badenes G, Pruneri V (2009) Highly sensitive sensors based on photonic crystal fiber modal interferometers. J Sens 2009

27. Kim B, Kim T-H, Cui L, Chung Y (2009) Twin core photonic crystal fiber for in-line Mach-Zehnder interferometric sensing applications. Opt Express 17 (18):15502-15507

28. Zeng S, Hu S, Xia J, Anderson T, Dinh X-Q, Meng X-M, Coquet P, Yong K-T (2015) Graphene–MoS_2 hybrid nanostructures enhanced surface plasmon resonance biosensors. Sensors and Actuators B: Chemical 207:801-810

29. Ilinykh V, Matyushkin L Sol-gel fabrication of one-dimensional photonic crystals with predicted transmission spectra. In: Journal of Physics: Conference Series, 2016. vol 1. IOP Publishing, p 012008

30. Shaban M, Ahmed AM, Abdel-Rahman E, Hamdy H (2017) Tunability and sensing properties of plasmonic/1D photonic crystal. Sci Rep 7:41983

31. Patrini M, Galli M, Belotti M, Andreani L, Guizzetti G, Pucker G, Lui A, Bellutti P, Pavesi L (2002) Optical response of one-dimensional (Si/SiO_2) m photonic crystals. J Appl Phys 92 (4):1816-1820

32. Bouaziz L, Nachi K, Gamra D, Lejeune M, Zeinert A, Zellama K, Bouchriha H (2015) Experimental evidence of the photonic bandgap and defect effect in $Si\text{-}SiO_2$ multilayer structures. Cryst Res Technol 50 (1):77-84

33. Wu L, Jia Y, Jiang L, Guo J, Dai X, Xiang Y, Fan D (2016) Sensitivity improved SPR biosensor based on the MoS_2/graphene–aluminum hybrid structure. J Lightwave Technol 35 (1):82-87

34. Aly AH (2008) Metallic and superconducting photonic crystal. J Supercond Nov Magn 21 (7):421

35. Aly AH, Zaky ZA, Shalaby AS, Ahmed AM, Vigneswaran D (2020) Theoretical study of hybrid multifunctional one-dimensional photonic crystal as a flexible blood sugar sensor. Phys Scr 95 (3):035510

36. Aly AH, Ryu S-W, Wu C-J (2008) Electromagnetic wave propagation characteristics in a one-dimensional metallic photonic crystal. J Nonlinear Opt Phy 17 (03):255-264

37. Aly AH, Elsayed HA (2012) Defect mode properties in a one-dimensional photonic crystal. Physica B 407 (1):120-125

38. O'Sullivan F, Celanovic I, Jovanovic N, Kassakian J, Akiyama S, Wada K (2005) Optical characteristics of one-dimensional Si/SiO_2 photonic crystals for thermophotovoltaic applications. J Appl Phys 97 (3):033529

39. Aly A, Ghany S-SA, Fadlallah M, Salman F, Kamal B (2015) Transmission and temperature sensing characteristics of a binary and ternary photonic band gap. J Nanoelectron Optoelectron 10 (1):9-14

40. Aly AH, Ismaeel M, Abdel-Rahman E (2012) Comparative study of the one-dimensional dielectric and metallic photonic crystals. OPJ 2 (02):105

41. Quan X, Fry ES (1995) Empirical equation for the index of refraction of seawater. Appl Optics 34 (18):3477-3480

42. Kravets V, Schedin F, Jalil R, Britnell L, Gorbachev R, Ansell D, Thackray B, Novoselov K, Geim A, Kabashin AV (2013) Singular phase nano-optics in plasmonic metamaterials for label-free single-molecule detection. Nature Materials 12 (4):304-309

43. Aly AH, Zaky ZA (2019) Ultra-sensitive photonic crystal cancer cells sensor with a high-quality factor. Cryogenics 104:102991

44. Liu Y, Wang S, Biswas P, Palit P, Zhou W, Sun Y (2019) Optofluidic vapor sensing with free-space coupled 2D photonic crystal slabs. Sci Rep 9 (1):4209

45. Zaky ZA, Ahmed AM, Shalaby AS, Aly AH (2020) Refractive index gas sensor based on the Tamm state in a one-dimensional photonic crystal: Theoretical optimisation. Sci Rep 10 (1):9736

46. Peng Y, Hou J, Huang Z, Lu Q (2012) Temperature sensor based on surface plasmon resonance within selectively coated photonic crystal fiber. Appl Optics 51 (26):6361-6367

47. Liao Y, Wang J, Yang H, Wang X, Wang S (2015) Salinity sensing based on microfiber knot resonator. Sens Actuator A-Phys 233:22-25

48. Wang Y, Huang Q, Zhu W, Yang M, Lewis E (2018) Novel optical fiber SPR temperature sensor based on MMF-PCF-MMF structure and gold-PDMS film. Opt Express 26 (2):1910-1917

49. Alam MS, Akter S, Paul BK, Ahmed K, Vigneswaran D, Aktar MN (2019) FEM based highly sensitive dual-core temperature sensor: design and analysis. OSA Continuum 2 (9):2581-2592

Figures

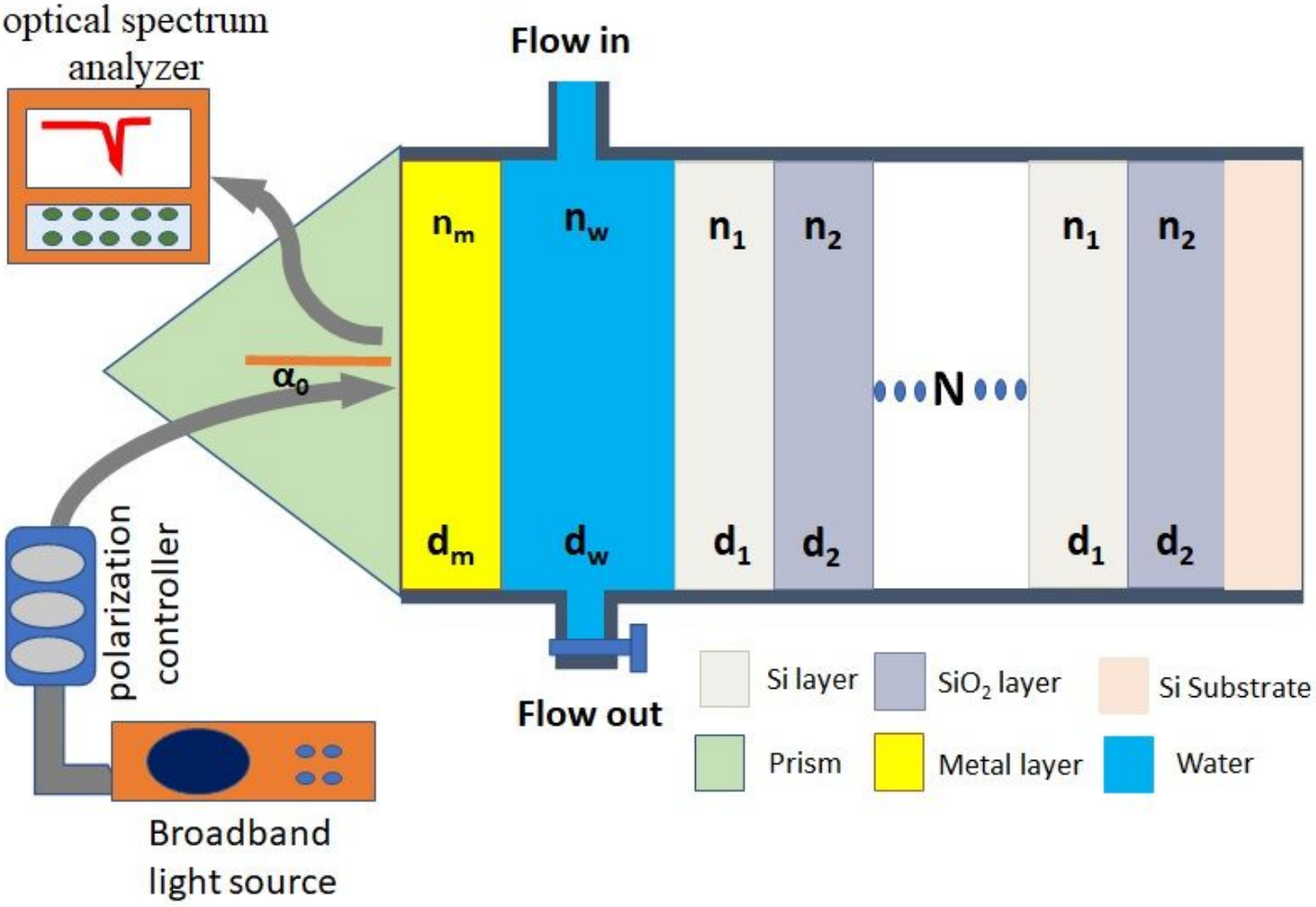

Figure 1

Schematic illustration and experimental setup of the suggested sensor consisting of prism/Au/ water/(Si/SiO_2)N/Si.

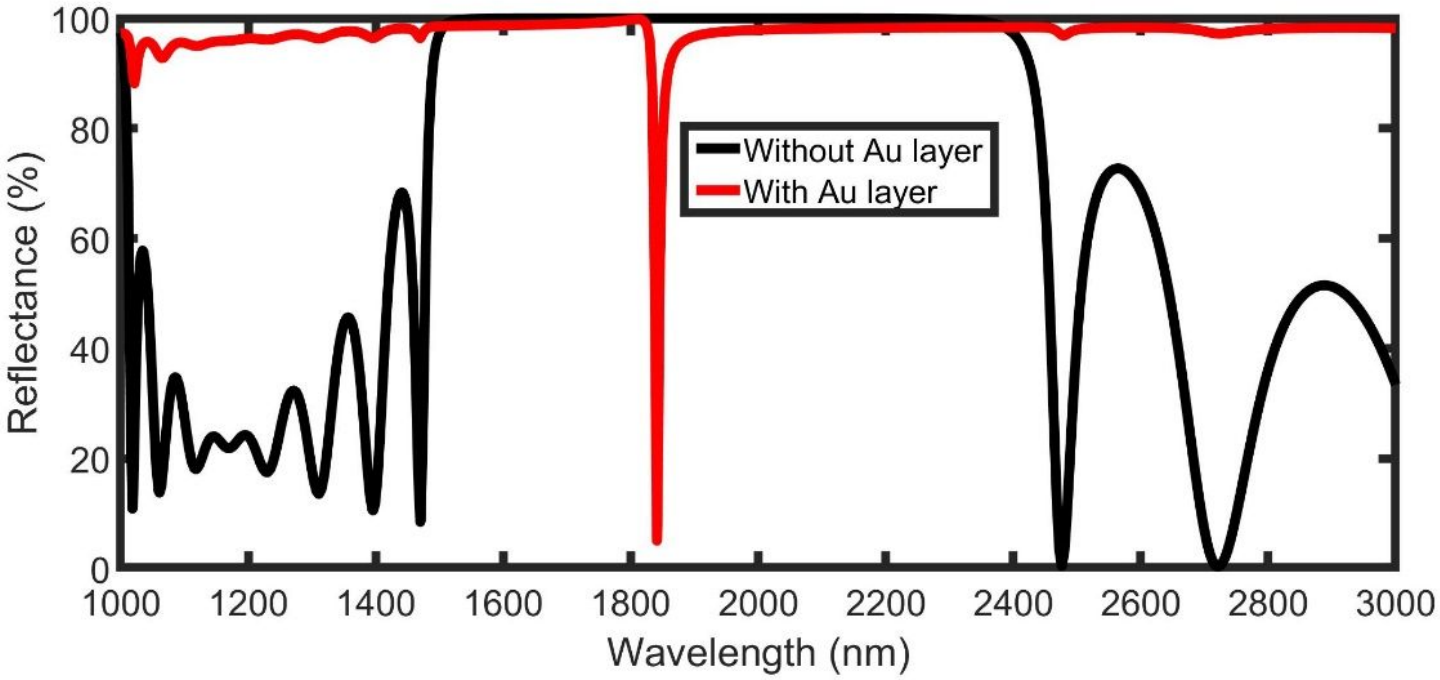

Figure 2

Reflectance spectra for prism/water/(Si/SiO_2)N/Si and prism/Au/ water/(Si/SiO_2)N/Si versus the wavelength with α0=0˚, N=8, dw=700 nm, Cs= 0 %, T=25 ˚C, and dm=25 nm.

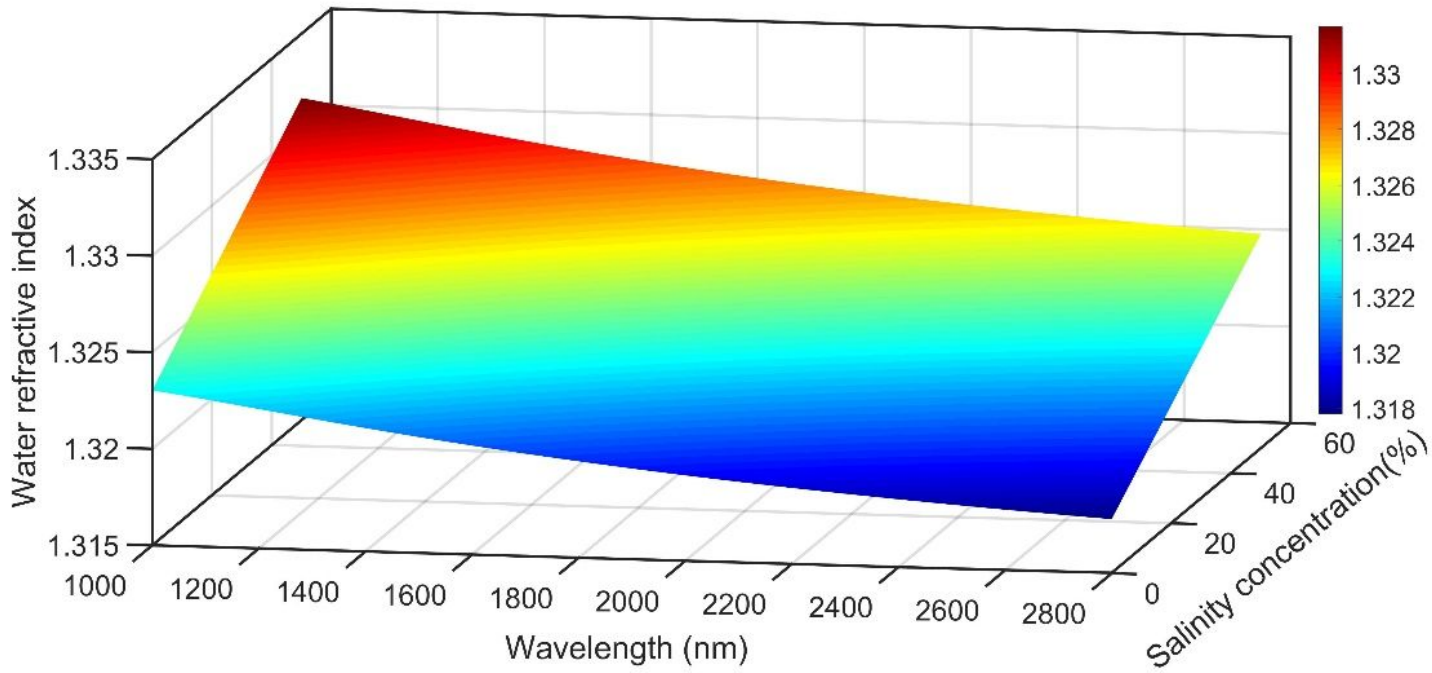

Figure 3

Dependence of water refractive index on both wavelength and salinity concentration at room temperature (25 ˚C).

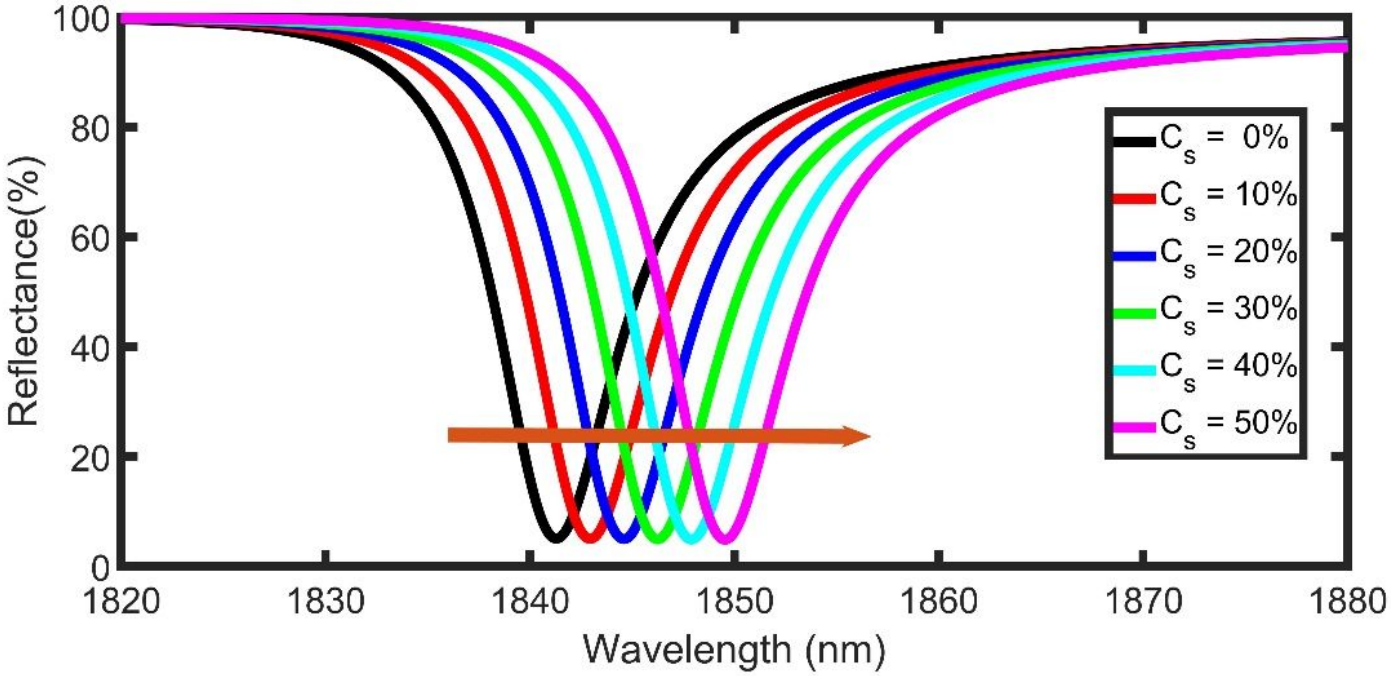

Figure 4

Reflectance spectra for prism/Au/water/(Si/SiO2)N/Si as a function of the wavelength at different salinity concentrations with α0=0˚, N=8, dw=700 nm, T=25 ˚C, and dm=25 nm.

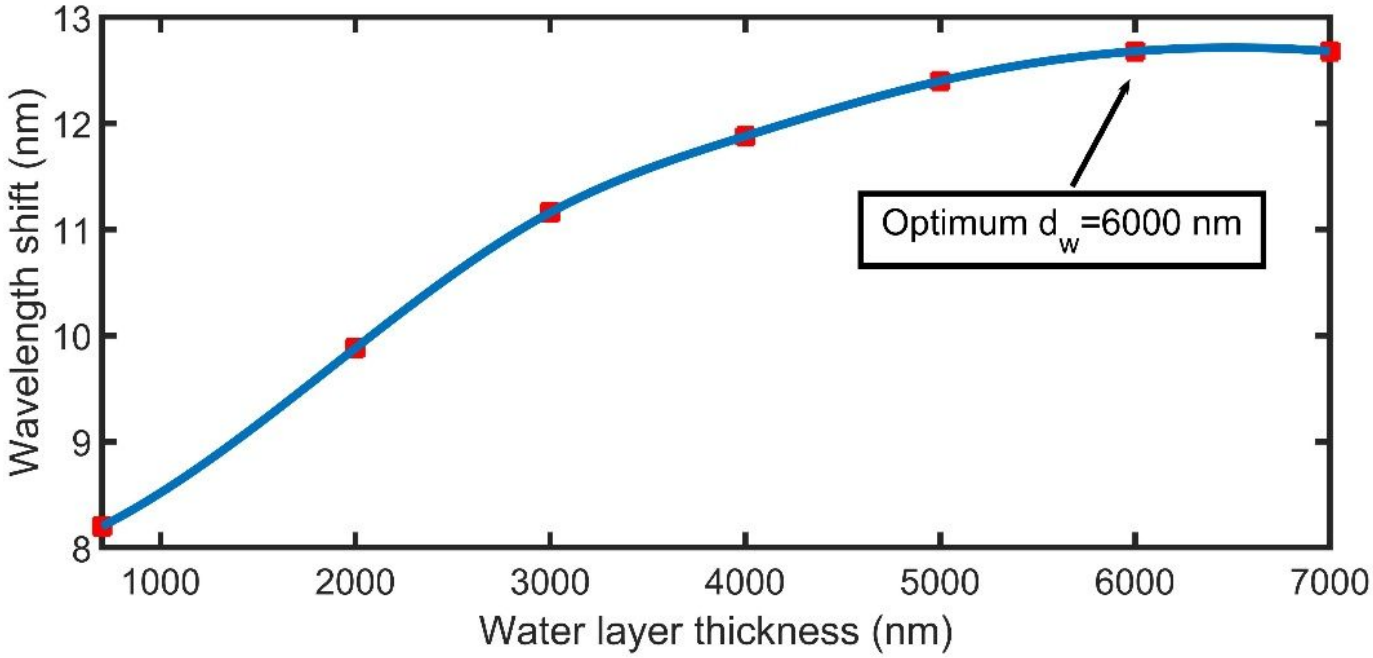

Figure 5

The relation between the thickness of the water layer and wavelength shift at N = 8, dm = 25 nm, T=25 ˚C, and α0=0˚.

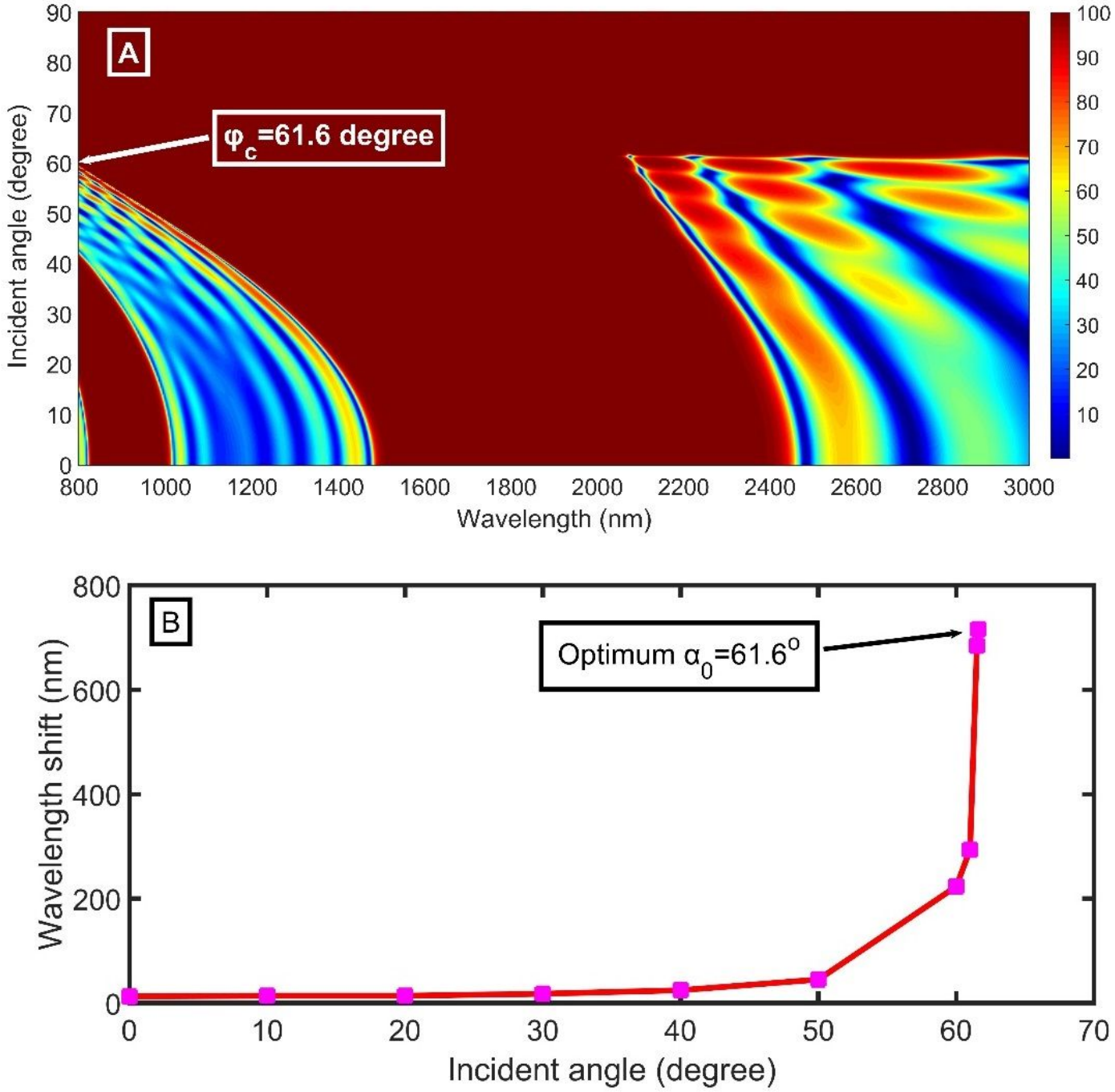

Figure 6

(A) The variation of reflectance as a function of wavelength and incident angle. (B) The relation between the incident angle and wavelength shift at N = 8, dm= 25 nm, dw= 6000 nm, and T=25 ˚C.

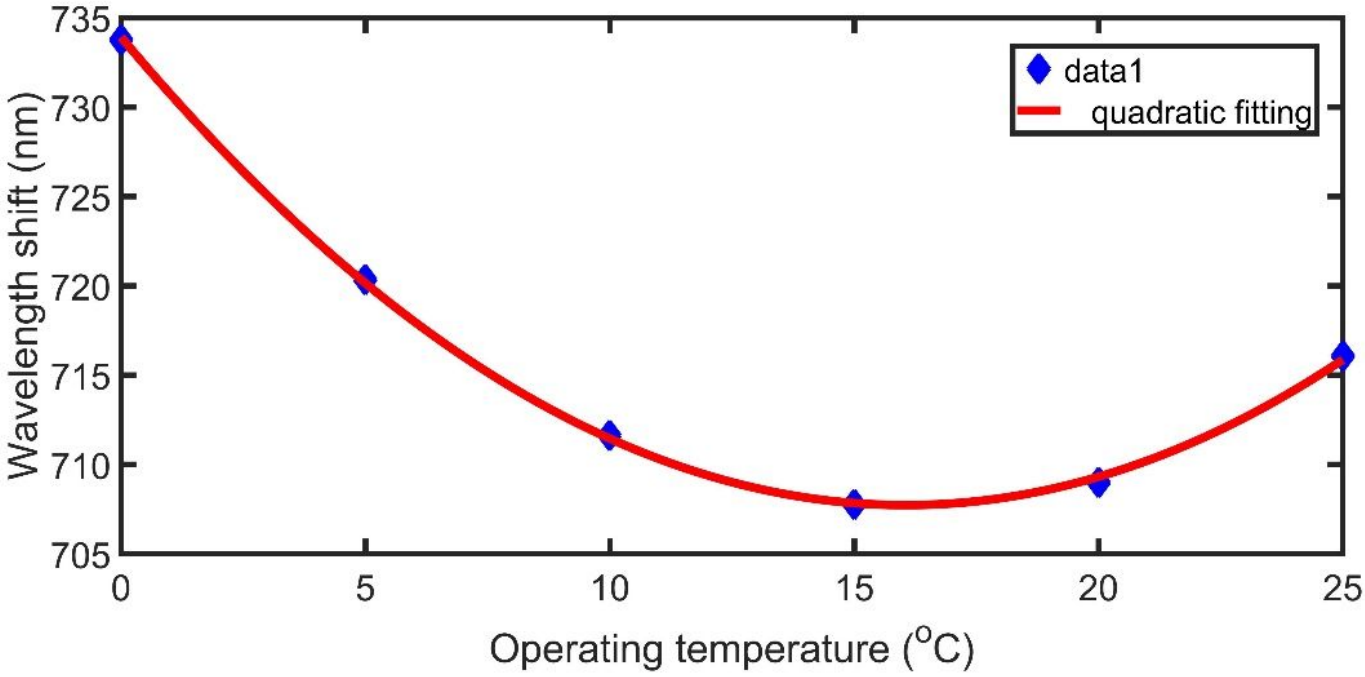

Figure 7

The effect of operating temperature on the performance of the salinity sensor at N = 8, dm= 25 nm, dw= 6000 nm, and α0=61.6˚.

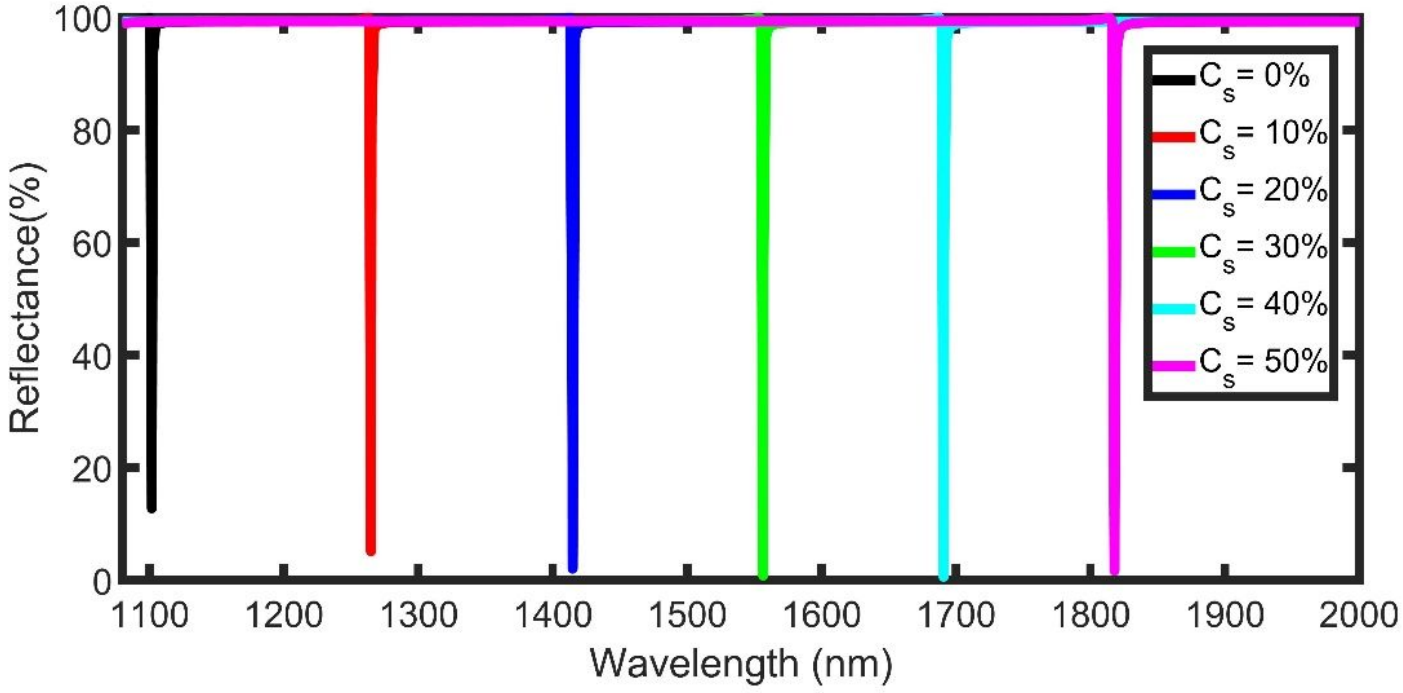

Figure 8

Reflectance of the salinity sensor at α0=61.6˚, N=8, dw=6000 nm, T=25 ˚C, and dm=25 nm.

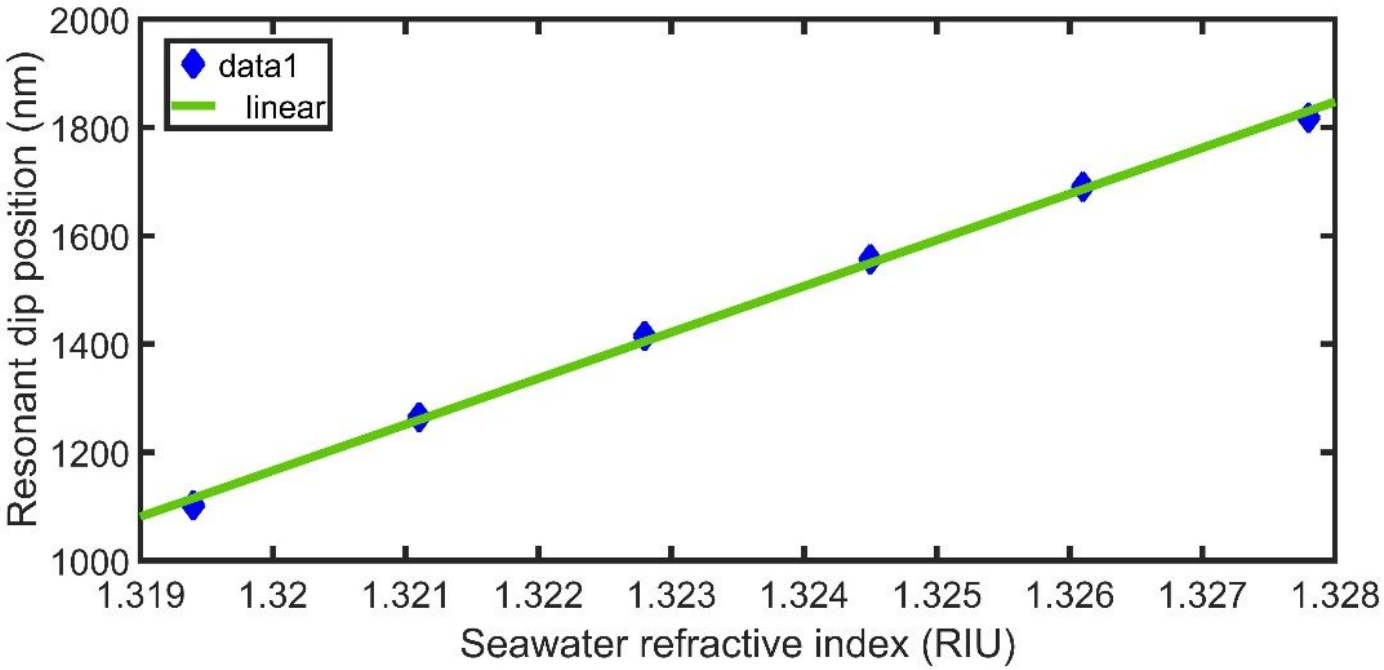

Figure 9

The linear relation between the refractive index of seawater and resonant dip position at optimum conditions.

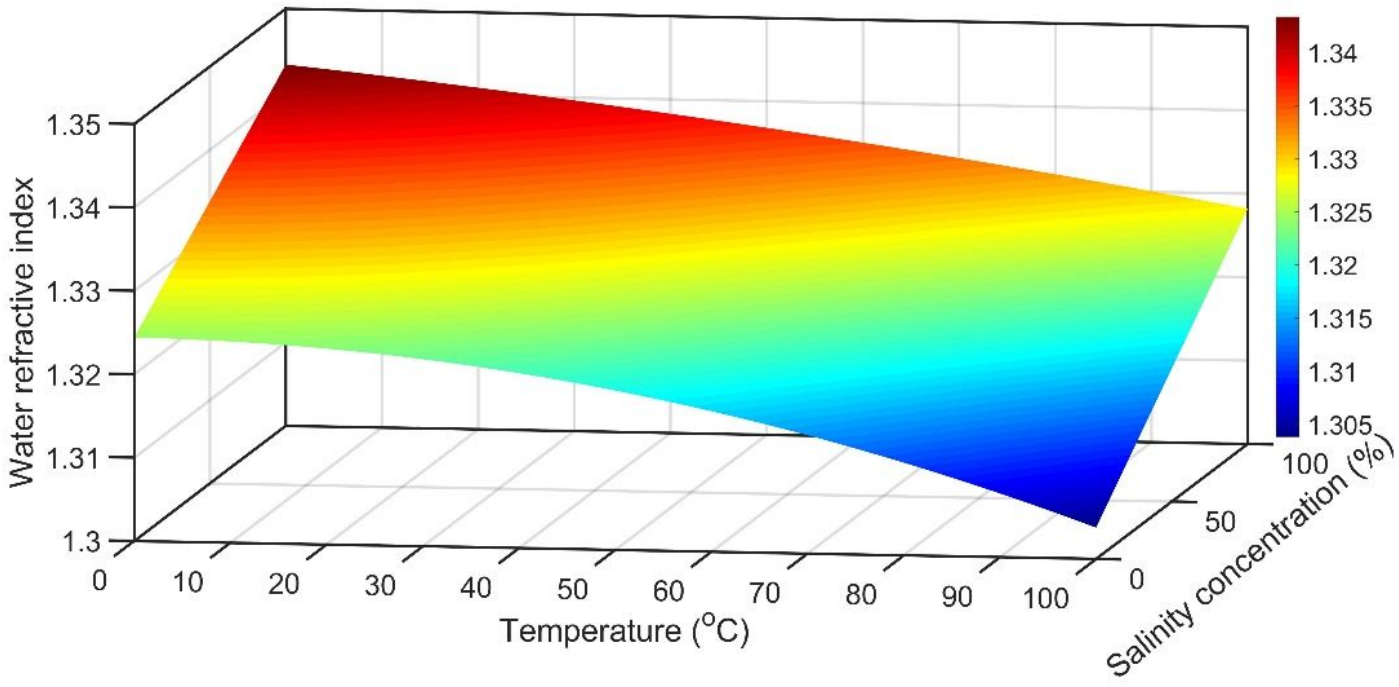

Figure 10

Dependence of water refractive index on both temperature and salinity concentration at a wavelength of 1000 nm.

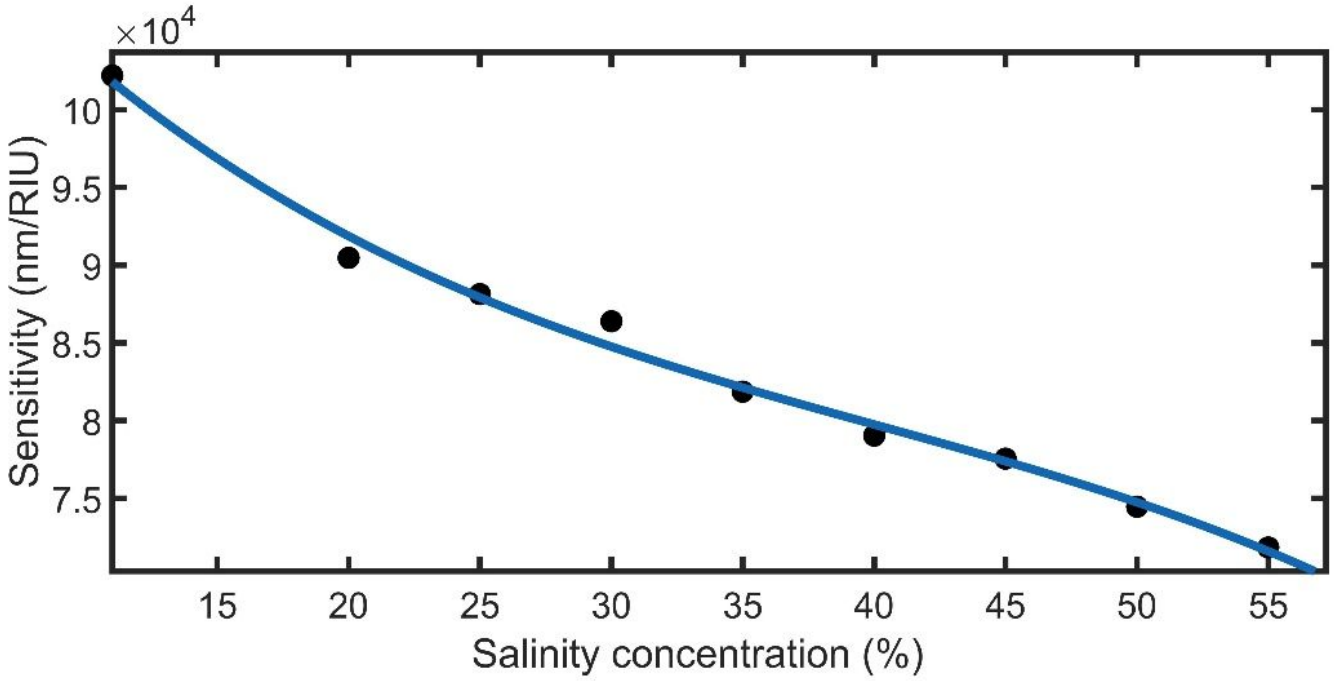

Figure 11

The effect of salinity concentration on the sensitivity of the temperature sensor at the optimum conditions

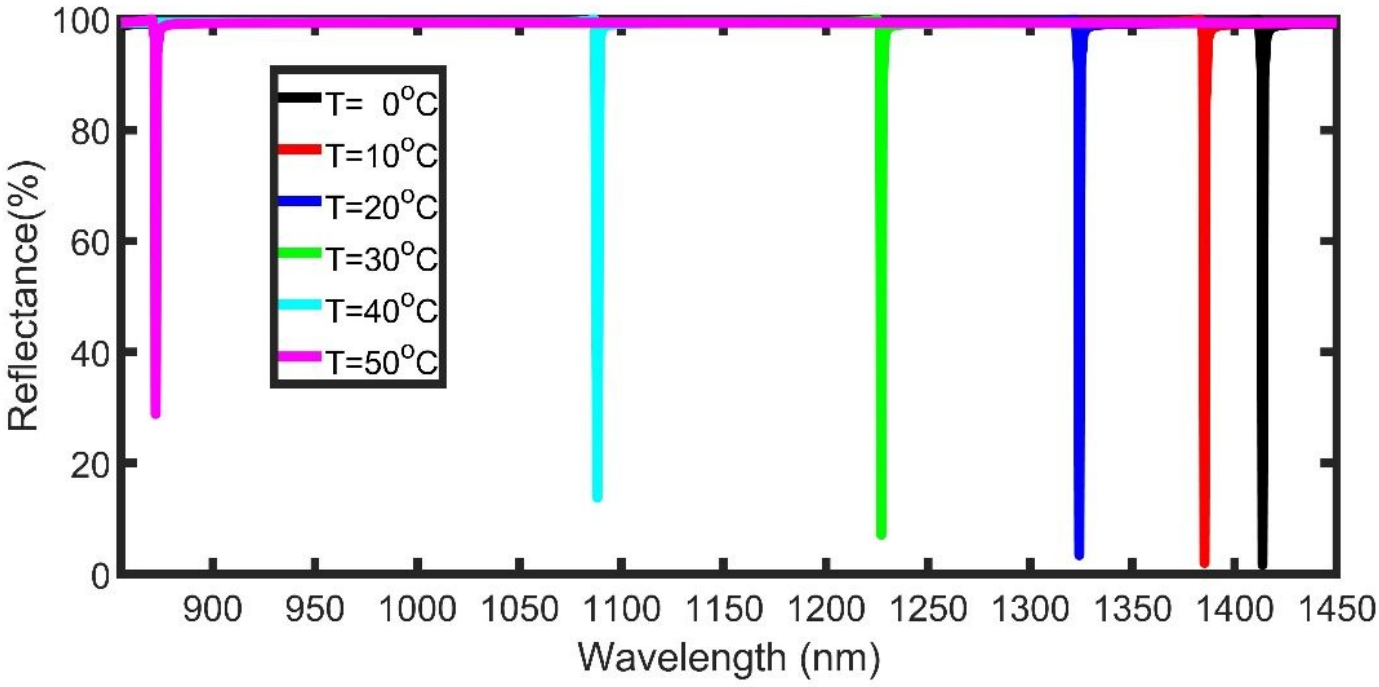

Figure 12

Reflectance spectra of the proposed structure as a temperature sensor as a function of the wavelength at different Temperatures with α0 =61.6°, N=8, dw=6000 nm, Cs=11 %, and dm=25 nm.

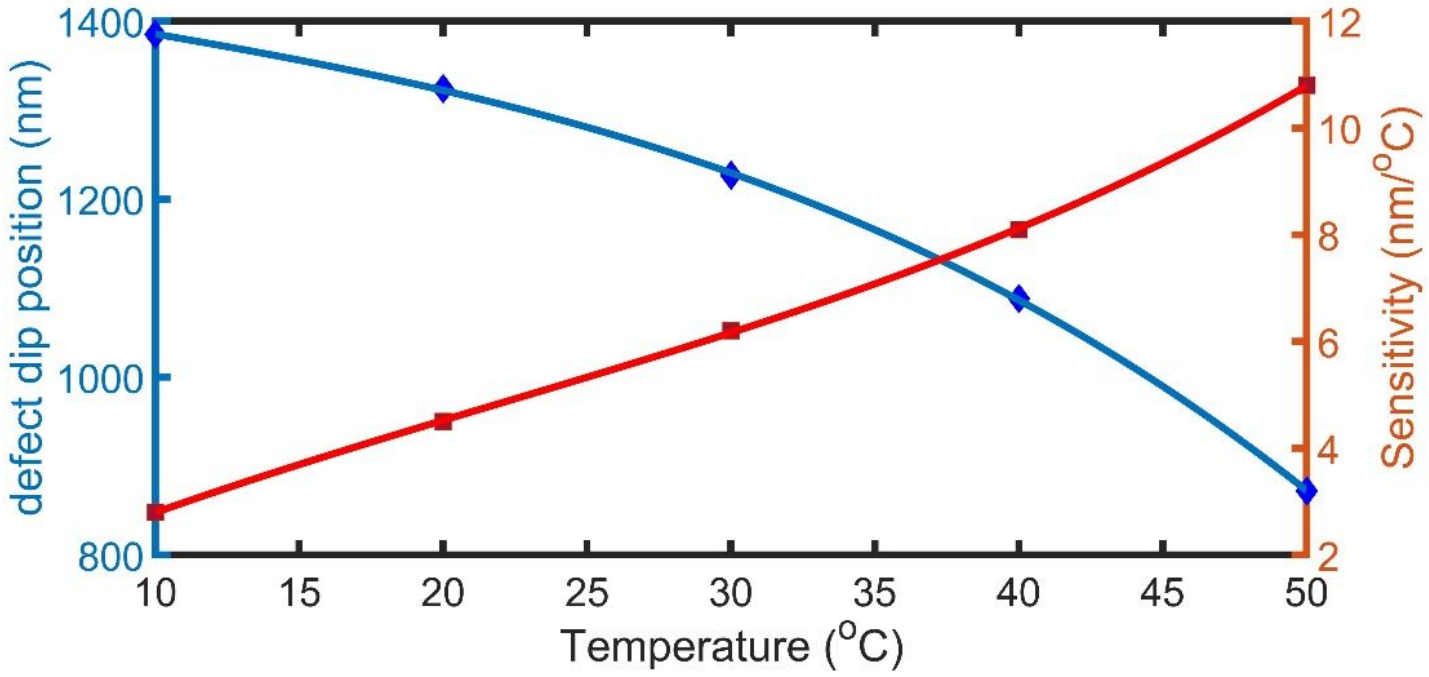

Figure 13

defect dip position and sensitivity of the proposed temperature sensor as a function of temperature at optimum conditions.